

THE HERA-19 COMMISSIONING ARRAY: DIRECTION DEPENDENT EFFECTS

SAUL A. KOHN,¹ JAMES E. AGUIRRE,¹ PAUL LA PLANTE,¹ TASHALEE S. BILLINGS,¹ PAUL M. CHICHURA,¹ AUSTIN F. FORTINO,¹ AMY S. IGARASHI,^{1,2} ROSHAN K. BENEFO,¹ SAMAVARTI GALLARDO,^{1,3} ZACHARY E. MARTINOT,¹ CHUNEETA D. NUNHOKEE,^{4,1} NICHOLAS S. KERN,⁵ PHILIP BULL,⁶ ADRIAN LIU,^{5,7} PAUL ALEXANDER,⁸ ZAKI S. ALI,⁵ ADAM P. BEARDSLEY,^{9,10} GIANNI BERNARDI,^{11,4,12} JUDD D. BOWMAN,⁹ RICHARD F. BRADLEY,¹³ CHRIS L. CARILLI,^{14,8} CARINA CHENG,⁵ DAVID R. DEBOER,⁵ ELOY DE LERA ACEDO,⁸ JOSHUA S. DILLON,^{5,10} AARON EWALL-WICE,^{15,16} GCOBISA FADANA,¹⁷ NICOLAS FAGNONI,⁸ RANDALL FRITZ,¹⁷ STEVE R. FURLANETTO,¹⁸ BRIAN GLENDENNING,¹⁴ BRADLEY GREIG,¹⁹ JASPER GROBBELAAR,¹² BRYNA J. HAZELTON,^{20,21} JACQUELINE N. HEWITT,²² JACK HICKISH,⁵ DANIEL C. JACOBS,⁹ AUSTIN JULIUS,¹² MACCALVIN KARISEB,¹² MATTHEW KOLOPANIS,^{23,9} TELALO LEKALAKE,¹² ANITA LOOTS,¹² DAVID MACMAHON,⁵ LOURENCE MALAN,¹² CRESSHIM MALGAS,¹² MATTHYS MAREE,¹² NATHAN MATHISON,¹² EUNICE MATSETELA,¹² ANDREI MESINGER,¹⁹ MIGUEL F. MORALES,²⁰ ABRAHAM R. NEBEN,²² BOJAN NIKOLIC,⁸ AARON R. PARSONS,⁵ NIPANJANA PATRA,⁵ SAMANTHA PIETERSE,¹² JONATHAN C. POBER,²⁴ NIMA RAZAVI-GHODS,⁸ JON RINGUETTE,²⁰ JAMES ROBNETT,¹⁴ KATHRYN ROSIE,¹² RADDWINE SELL,¹² CRAIG SMITH,¹² ANGELO SYCE,¹² MAX TEGMARK,²² NITHYANANDAN THYAGARAJAN,^{14,9,25} PETER K. G. WILLIAMS,²⁶ AND HAOXUAN ZHENG²²

¹ Department of Physics and Astronomy, University of Pennsylvania, Philadelphia, PA 19104 USA

² Department of Astronomy, San Diego State University, San Diego, CA 92182 USA

³ California State University of Los Angeles, 5151 State University Dr, Los Angeles, CA 90032 USA

⁴ Department of Physics and Electronics, Rhodes University, PO Box 94, Grahamstown, 6140, South Africa

⁵ Department of Astronomy, University of California, Berkeley, CA

⁶ Philip Bull, School of Physics & Astronomy, Queen Mary University of London, Mile End Road, London E1 4NS, UK

⁷ Hubble Fellow

⁸ Cavendish Astrophysics, University of Cambridge, Cambridge, UK

⁹ School of Earth and Space Exploration, Arizona State University, Tempe, AZ

¹⁰ NSF Astronomy and Astrophysics Postdoctoral Fellow

¹¹ INAF-Istituto di Radioastronomia, via Gobetti 101, 40129, Bologna, Italy

¹² SKA SA, 3rd Floor, The Park, Park Road, Pinelands, 7405, South Africa

¹³ National Radio Astronomy Observatory, Charlottesville, VA

¹⁴ National Radio Astronomy Observatory, Socorro, NM

¹⁵ Jet Propulsion Laboratory, 4800 Oak Grove Dr, Pasadena, CA

¹⁶ Dunlap Institute for Astronomy and Astrophysics, Toronto, Ontario, Canada

¹⁷ SKA-SA, Cape Town, South Africa

¹⁸ Department of Physics and Astronomy, University of California, Los Angeles, CA

¹⁹ Scuola Normale Superiore, Pisa, Italy

²⁰ Department of Physics, University of Washington, Seattle, WA

²¹ eScience Institute, University of Washington, Seattle, WA

²² Department of Physics, Massachusetts Institute of Technology, Cambridge, MA

²³ Department of Physics, Arizona State University, Tempe, AZ

²⁴ Department of Physics, Brown University, Providence, RI

²⁵ Jansky Fellow

²⁶ Harvard-Smithsonian Center for Astrophysics, Cambridge, MA

ABSTRACT

Corresponding author: James E. Aguirre
jaguirre@sas.upenn.edu

Foreground power dominates the measurements of interferometers that seek a statistical detection of highly-redshifted HI emission from the Epoch of Reionization (EoR). The chromaticity of the instrument creates a boundary in the Fourier transform of frequency (proportional to k_{\parallel}) between spectrally smooth emission, characteristic of the strong synchrotron foreground (the “wedge”), and the spectrally structured emission from HI in the EoR (the “EoR window”). Faraday rotation can inject spectral structure into otherwise smooth polarized foreground emission, which through instrument effects or miscalibration could possibly pollute the EoR window. For instruments pursuing a “foreground avoidance” strategy of simply measuring in the EoR window, and not attempting to model and remove foregrounds, as is the plan for the first stage of the Hydrogen Epoch of Reionization Array (HERA), characterizing the intrinsic instrument polarization response is particularly important. Using data from the HERA 19-element commissioning array, we investigate the polarization response of this new instrument in the power spectrum domain. We perform a simple image-based calibration based on the unpolarized diffuse emission of the Global Sky Model, and show that it achieves qualitative redundancy between the nominally-redundant baselines of the array and reasonable amplitude accuracy. We construct power spectra of all fully polarized coherencies in all pseudo-Stokes parameters, and discuss the achieved isolation of foreground power due to the intrinsic spectral smoothness of the foregrounds, the instrument chromaticity, and the calibration. We compare to simulations based on an unpolarized diffuse sky model and detailed electromagnetic simulations of the dish and feed, confirming that in Stokes I, the calibration does not add significant spectral structure beyond that expected from the interferometer array configuration and the modeled primary beam response. Further, this calibration is stable over the 8 days of observations considered. Excess power is seen in the power spectra of the linear polarization Stokes parameters which is not easily attributable to leakage via the primary beam, and results from some combination of residual calibration errors and actual polarized emission. Stokes V is found to be highly discrepant from the expectation of zero power, strongly pointing to the need for more accurate polarized calibration.

Keywords: cosmology: observations - dark ages, reionization, first stars – instrumentation: interferometers – techniques: interferometric – polarization

1. INTRODUCTION

Many low-frequency (50 – 200 MHz) radio interferometers (e.g. LOFAR¹, MWA², PAPER³, HERA⁴) around the world are seeking to detect brightness-temperature fluctuations of neutral hydrogen during the Epoch of Reionization (EoR; for an overview see Furlanetto et al. (2006)). Such a detection is predicted to be rich in information about the astrophysics and cosmology of the high-redshift ($\sim 7 < z < 14$) Universe. The HI brightness-temperature fluctuations are not only intrinsically faint but also hidden by foreground emission. Foreground emission, predominantly in the form of galactic and extragalactic synchrotron emission, is many orders of magnitude more powerful than the cosmological signal (e.g. Bernardi et al. 2009a; Pober et al. 2013; Dillon et al. 2014).

Most foreground emission is due to synchrotron emission, which is spectrally smooth. The instrumental response of an interferometer is inherently chromatic, and the cosmological signal is spectrally structured. In sum, this leads to the property that Fourier transforming the interferometric measurement along the frequency axis delineates a boundary in the \mathbf{k} -space between the **spectrally smooth** foregrounds (in the “wedge”) and the cosmological HI signal (in the “EoR window”) (Datta et al. 2010; Morales et al. 2012; Parsons et al. 2012b,a; Trott et al. 2012; Vedantham et al. 2012; Pober et al. 2013; Thyagarajan et al. 2013; Pober et al. 2014; Liu et al. 2014a,b; Dillon et al. 2015b,a; Thyagarajan et al. 2015a,b). Thermal noise is present throughout this space, and dominates the EoR window in any single observation. Detection of the EoR thus requires long observing seasons, precision calibration, and suppression of instrument systematics.

The cosmological HI signal is strongly unpolarized (?). However, polarized synchrotron radiation represents a potential foreground contaminant capable of leaking into the EoR window. At low frequencies, Faraday rotation can impart significant spectral structure to polarized emission (e.g. Moore et al. 2013). This polarized signal is able to ‘leak’ into unpolarized measurements due to miscalibration and instrumental effects (Carozzi & Woan 2009; Geil et al. 2011; Moore et al. 2013; Asad et al. 2015, 2016; Kohn et al.

2016; Nunhokee et al. 2017), contaminating the EoR window.

It is important to constrain intrinsic and leaked polarized signal for any HI intensity mapping experiment. The objective of this paper is an exploration of eight nights of data from the Hydrogen Epoch of Reionization Array (HERA) 19-element commissioning array, coupled with simulations of the instrument, in order to **characterize the polarized response of this interferometer**. One of the more difficult features of an interferometer to characterize is the frequency- and direction-dependent polarized antenna response, which is important for characterizing polarized-to-unpolarized leakage in the wedge/window paradigm (Moore et al. 2017; Nunhokee et al. 2017; Martinot et al. 2018). In this work, we were primarily sensitive to leakage in the unpolarized-to-polarized direction. Due to the symmetry of leakage modes (elaborated upon in Section 2), this still represents a useful constraint on the future problem of polarized-to-unpolarized leakage contaminating the EoR signal. While we use cosmological power spectra as a diagnostic of the data, the goal of this paper is not to obtain new upper limits on the EoR power spectrum, but simply to integrate deep enough to test models of the instrument’s spectral response against simulations.

This work is organized as follows: in Section 2 we review the theory behind polarization leakage into unpolarized signal and present the polarized primary beam model for the HERA commissioning array. In Section 3 we describe the HERA data that we used, its calibration, and reduction to power spectra. We present our results, and discuss the implications in Section 4, and conclude in Section 12.

We assume the cosmological parameters reported by Planck Collaboration et al. (2016) throughout.

2. LEAKAGE MODES

A radio interferometer measures correlations of voltages. Viewed in transmission, a dipole arm of antenna i radiates a far-field electric field pattern

$$\vec{E}_i(\hat{s}, \nu) = E_{i,\theta}(\nu)\hat{\theta} + E_{i,\phi}(\nu)\hat{\phi} \quad (1)$$

where $(\hat{\theta}, \hat{\phi})$ define an orthogonal coordinate system on the sphere. These far-field beam patterns, by the reciprocity theorem, define the response of the feed to an electric field from infinity in the direction (θ, ϕ) .

We may choose to express the electric field response in Right Ascension and Declination basis (unit vectors

¹ www.lofar.org

² www.mwatelescope.org

³ eor.berkeley.edu

⁴ www.reionization.org

$\hat{e}_\alpha, \hat{e}_\delta$), allowing us to express the coherency tensor field

$$\begin{aligned} \mathcal{C} = & \langle E_\delta^* E_\delta \rangle \hat{e}_\delta \otimes \hat{e}_\delta + \langle E_\alpha^* E_\delta \rangle \hat{e}_\alpha \otimes \hat{e}_\delta \\ & + \langle E_\delta^* E_\alpha \rangle \hat{e}_\delta \otimes \hat{e}_\alpha + \langle E_\alpha^* E_\alpha \rangle \hat{e}_\alpha \otimes \hat{e}_\alpha \end{aligned} \quad (2)$$

where we have dropped the explicit (\hat{s}, ν) dependence of the fields. By definition, the coherency field is specified by the Stokes parameters

$$\mathcal{C} = \begin{pmatrix} I(\hat{s}, \nu) + Q(\hat{s}, \nu) & U(\hat{s}, \nu) - iV(\hat{s}, \nu) \\ U(\hat{s}, \nu) + iV(\hat{s}, \nu) & I(\hat{s}, \nu) - Q(\hat{s}, \nu) \end{pmatrix}. \quad (3)$$

Each polarized feed p of antenna i responds to incident radiation from direction $(\hat{\theta}, \hat{\phi})$ with a complex vector antenna pattern

$$\vec{A}_i^p(\hat{s}, \nu) = A_{i,\theta}^p(\hat{s}, \nu)\hat{\theta} + A_{i,\phi}^p(\hat{s}, \nu)\hat{\phi}. \quad (4)$$

The antenna patterns can be written as components of a direction-dependent Jones matrix for a dipole feed i with arms p and q :

$$\mathcal{J}_i = \begin{pmatrix} A_{i,\theta}^p(\hat{s}, \nu) & A_{i,\phi}^p(\hat{s}, \nu) \\ A_{i,\theta}^q(\hat{s}, \nu) & A_{i,\phi}^q(\hat{s}, \nu) \end{pmatrix}. \quad (5)$$

We can then express the fully-polarized visibility equation for the correlation of feeds i and j as

$$V_{ij} = \int \mathcal{J}_i \mathcal{C} \mathcal{J}_j^\dagger \exp(-2\pi i \nu \vec{b} \cdot \hat{s}/c) d\Omega = \begin{pmatrix} V_{ij}^{nn} & V_{ij}^{ne} \\ V_{ij}^{en} & V_{ij}^{ee} \end{pmatrix} \quad (6)$$

where we have denoted dipole arms p and q as n and e , representing a configuration where the arms are oriented along the North-South and East-West directions, respectively.

Unless \mathcal{J} is both diagonal and **has, at any given point on the sphere, equal diagonal elements, there will be mixing or “leaking” of different Stokes parameters** together into each element of \mathcal{V} in a direction dependent way (Geil et al. 2011; Smirnov 2011a,b; Nunhokee et al. 2017).

2.1. Direction-Dependent Leakage

The cosmological signal of interest for 21cm cosmology studies is effectively unpolarized, and we therefore use the pseudo-Stokes⁵ I visibility to measure it (**e.g.**

⁵ We use “pseudo-Stokes” to refer to Stokes parameters formed from visibilities throughout this work, **to distinguish from true “Stokes parameters” defined in the image domain** by the IEEE (Ludwig 1973; van Straten et al. 2010).

Moore et al. 2013); this is defined $V^I = V^{nn} + V^{ee}$, which is the trace of \mathcal{V} :

$$\begin{aligned} V_{ij}^I(\nu) &= \text{Tr}(\mathcal{V}_{ij}) = \int \text{Tr}(\mathcal{J}_i \mathcal{C} \mathcal{J}_j^\dagger) \exp(-2\pi i \nu \vec{b} \cdot \hat{s}/c) d\Omega \\ &= \int (\mathcal{M}_{00} I + \mathcal{M}_{01} Q + \mathcal{M}_{02} U + \mathcal{M}_{03} V) \exp(-2\pi i \nu \vec{b} \cdot \hat{s}/c) d\Omega \end{aligned} \quad (7)$$

where I, Q, U and V are the true Stokes sky and are functions of direction and frequency, and $\mathcal{M}_{ab}(\hat{s}, \nu)$ are the instrumental Mueller matrix elements:

$$\mathcal{M}_{ab}(\hat{s}, \nu) = \text{Tr}(\sigma_a \mathcal{J} \sigma_b \mathcal{J}^\dagger) \quad (8)$$

and σ_i are the Pauli matrices (where the indices are reordered from the quantum mechanical convention to an order which gives the ordering of the Stokes vector as (I, Q, U, V) ; see, e.g., Shaw et al. 2015).

We simulated the HERA feed, faceted parabolic dish and analog signal chain using CST⁶ to generate the complex \vec{E} -field receptivity patterns, as described in Fagnoni & de Lera Acedo (2016) (also see public [HERA Memo #21](#)), and then formed \mathcal{J} and \mathcal{M} as described above. Examples of \mathcal{M}_{ij} at 120 MHz and 160 MHz (our low and high bands of interest; see Section 3.2) are shown in Figure 1, projected in the RA/Dec basis. Note that this basis has a singularity at the South Pole, leading to wide-field asymmetries in Q and U . Due to the large spread in dynamic ranges between \mathcal{M}_{00} , other diagonal terms, and off-diagonal terms, we use separate color maps for each. All of the dynamic ranges are normalized to the peak of \mathcal{M}_{00} , which is 1 at zenith. The off-diagonal terms are 2- to 8-orders of magnitude less than the diagonal terms.

The key for these matrices are the mappings of Stokes parameters into pseudo-Stokes visibilities, following

$$\mathcal{M}_{ab}(\hat{s}, \nu) = \begin{pmatrix} I \rightarrow V^I & I \rightarrow V^Q & I \rightarrow V^U & I \rightarrow V^V \\ Q \rightarrow V^I & Q \rightarrow V^Q & Q \rightarrow V^U & Q \rightarrow V^V \\ U \rightarrow V^I & U \rightarrow V^Q & U \rightarrow V^U & U \rightarrow V^V \\ V \rightarrow V^I & V \rightarrow V^Q & V \rightarrow V^U & V \rightarrow V^V \end{pmatrix} \quad (9)$$

where pseudo-Stokes visibilities are formed as:

$$\begin{pmatrix} V^I \\ V^Q \\ V^U \\ V^V \end{pmatrix} = \frac{1}{2} \begin{pmatrix} 1 & 0 & 0 & 1 \\ 1 & 0 & 0 & -1 \\ 0 & 1 & 1 & 0 \\ 0 & -i & i & 0 \end{pmatrix} \begin{pmatrix} V^{nn} \\ V^{ne} \\ V^{en} \\ V^{ee} \end{pmatrix}. \quad (10)$$

⁶ www.cst.com

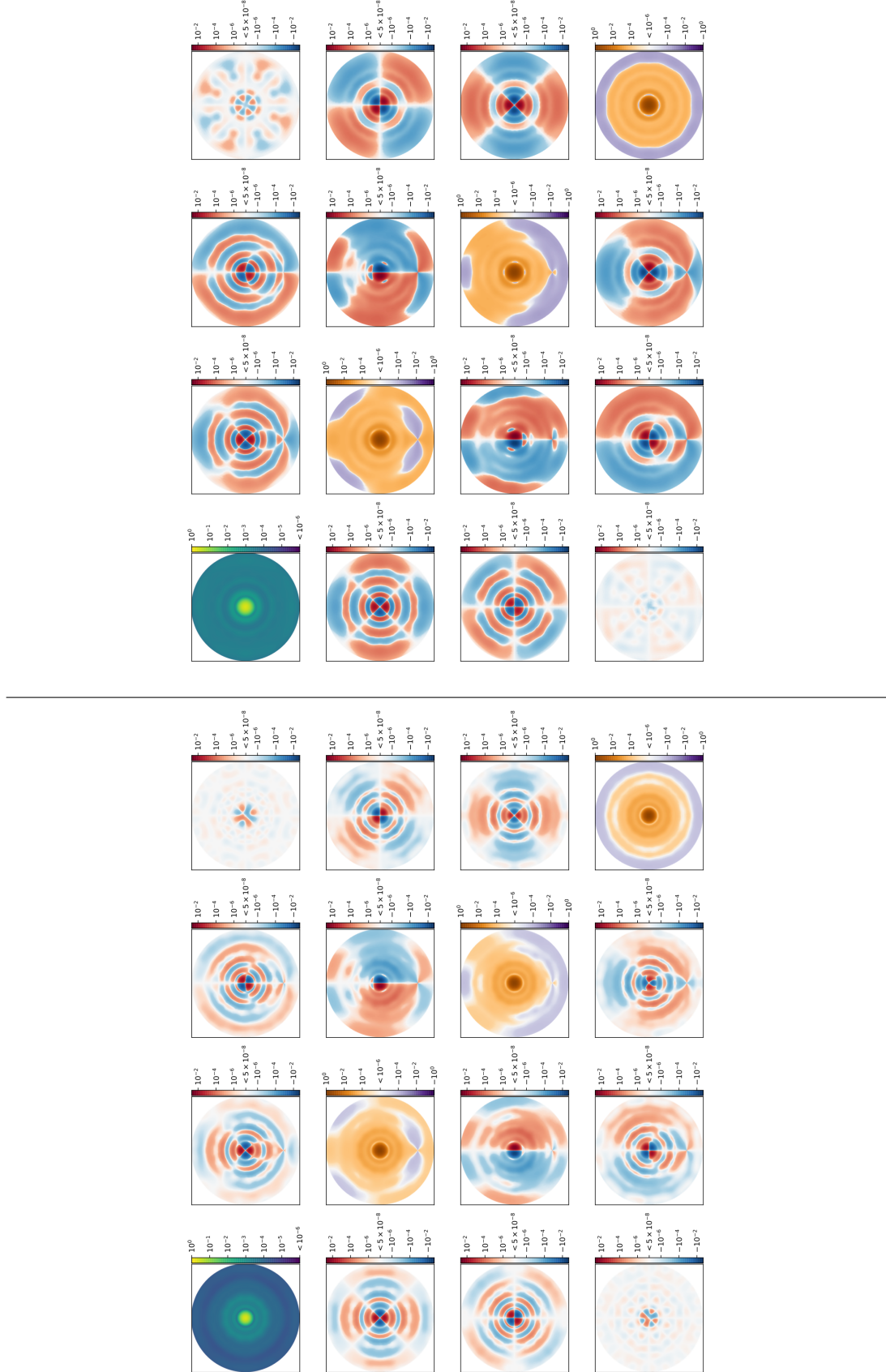


Figure 1. Simulations of the instrumental direction dependent Mueller matrix at 120 MHz and 160 MHz (*above* and *below*, respectively) projected into the RA, Dec basis. Color scales for frequencies are relative to the peak of \mathcal{M}_{00} (which itself is normalized to 1 at zenith). To account for the wide variety of dynamic ranges required to show detail, we use separate color maps for \mathcal{M}_{00} , diagonal, and off-diagonal terms. The off-diagonal terms are 2- to 8-orders of magnitude less than the diagonal terms. For a key to these matrices, see Equation 9.

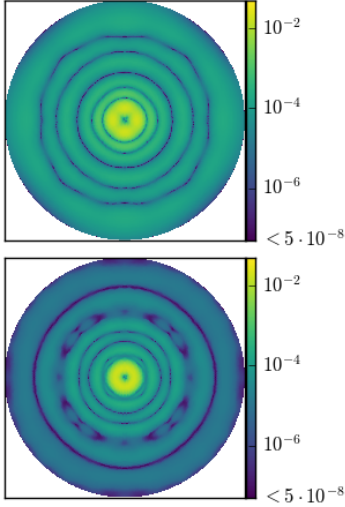


Figure 2. The magnitude of the linear polarization leakage beam given by $\mathcal{M}_p = \sqrt{\mathcal{M}_{IQ}^2 + \mathcal{M}_{IU}^2}$, or the middle two entries of the top row of Figure 1, at 120 MHz and 160 MHz (above and below, respectively).

At low frequencies and the large scales probed by many low frequency interferometers, Stokes I is extremely bright compared to the other Stokes parameters (Bernardi et al. 2009b, 2010; Jelić et al. 2014, 2015; Asad et al. 2015; Kohn et al. 2016; Lenc et al. 2017; Moore et al. 2017). Moreover, only a few polarized point sources have been observed at frequencies below 300 MHz (Bernardi et al. 2013; Asad et al. 2016; Lenc et al. 2017). Farnes et al. (2014) showed evidence for systematic depolarization of steep-spectrum point sources towards low frequencies, causing low polarization fractions ($\ll 1\%$) below 300 MHz.

The “linear polarization leakage beam” is shown for the two central frequencies of this analysis in Figure 2. This quantity is the magnitude of the spin-2 function $\mathcal{M}_{IQ} + i\mathcal{M}_{IU}$ and represents the amplitude of the direction-dependent leakage of Stokes Q and U into I.

These factors make the **first row of \mathcal{M}** , which represents $I \rightarrow V^I, V^Q, V^U, V^V$, the most interesting for low-frequency polarized power spectra, since with limited calibration we can expect leakage from Stokes I into the other Stokes parameters to dominate over Stokes Q, U, and V emission alone.

We produced simulations \mathcal{V} using our fully-polarized formalism for the HERA-19 commissioning array, described below, using an unpolarized model of the low frequency sky from the Global Sky Model (GSM; de Oliveira-Costa et al. 2008; Price 2016; Zheng et al. 2017) at the appropriate R.A. range to match our observations.

These simulations are based on the same source code as Martinot et al. (2018).

Forming power spectra from these visibilities allowed for a comparison of our data to a “leakage only” regime. We discuss the process for forming power spectra in Section 3.3, and the simulated power spectra are shown in comparison to those from data in Section 4.

2.2. Direction-Independent Leakage

In addition to the mixing of Stokes parameters due to the primary beam, it is possible to mix them in a direction independent way. Calibration errors are capable of leaking signal between pseudo-Stokes visibilities independent of the sky (Thompson et al. 2008). Again focusing on the $\{V^I, V^Q, V^U, V^V\}$ components of this leakage, we have:

- $V^I \rightarrow V^Q$ occurs through errors in calibrating the complex voltage gain factors for each dipole arm.
- $V^I \rightarrow V^U$ occurs through the sum of off-diagonal gain terms (D -terms; the receptivity of dipole arm “n” to an electric field vector aligned with arm “e” and vice versa).
- $V^I \rightarrow V^V$ occurs through the difference in D -terms between two feeds.

We detail how we obtain the direction-independent Jones terms in the next section.

3. OBSERVATIONS AND REDUCTION

In this work we used eight nights of observations from the HERA-19 commissioning array. HERA is a low-frequency interferometer composed of 14 m-diameter dishes arranged in a close-packed hexagonal array of 14.7 m spacing. The commissioning array consists of nineteen dishes (see Figure 3); HERA is being constructed in staged build-outs, and upon completion will consist of 350 dishes in a fractured hexagon configuration (see Dillon & Parsons 2016; DeBoer et al. 2017). A feed cage containing two dipole feeds (recycled from the PAPER array, see Parsons et al. 2010), oriented in North-South and East-West directions, was suspended above each dish (Neben et al. 2016; Ewall-Wice et al. 2016; Thyagarajan et al. 2016).

HERA only observes in drift-scan mode. The observations we used were eight nights, from Julian Date (JD) 2457548 to 2457555; LSTs 10.5 – 23 hr. Drift-scan visibilities were recorded every 10.7 seconds for 1024 evenly-spaced channels across the 100-200 MHz bandwidth. These data were divided into MIRIAD data sets

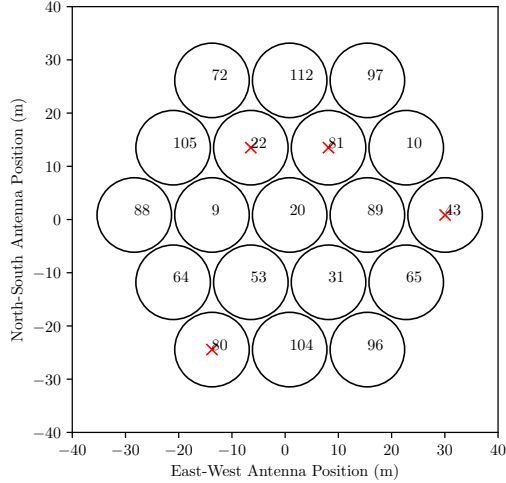


Figure 3. The configuration of the HERA-19 array. The perimeter of each dish is shown as a circle. A red “X” marks antennas that were identified during preprocessing and calibration as malfunctioning and were excluded from further analysis.

Table 1. Observational parameters used for this study.

Parameter	Value
Array location	30:43:17.5° S, 21:25:41.9° E
JD range	2457548 – 2457555
LST Range	10.6 – 22.6 hrs
Frequency range	115 – 185 MHz
Frequency resolution	97.6 kHz
Integration time	10.7 s
Element diameter	14.0 m
Number of elements	15
Shortest baseline	14.6 m
Longest baseline	58.4 m
At 150 MHz:	
Primary beam FWHM	9°
Synthesized beam FWHM	2°
SEFD per element	~ 5800 Jy

roughly 10 minutes long. A night’s observation lasted 12 hours in total (6pm to 6am South African Standard Time; SAST); of these we used the central 10 hours, to avoid the sun. **A summary of the instrument and observation parameters is given in Table 1.**

3.1. RFI Excision and Flagging

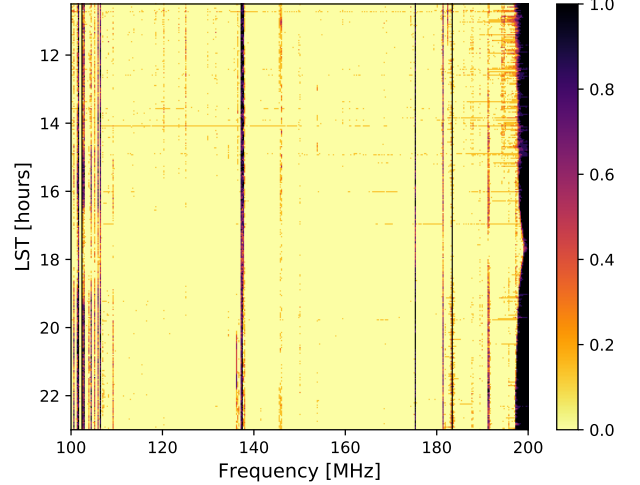


Figure 4. Fractional RFI flag occupancy per time and frequency over the eight days of observations. RFI was flagged on a per-(time,frequency) sample basis.

To identify samples contaminated by radio frequency interference (RFI), a two-dimensional median filter in time and frequency was applied to the visibility data to smooth out high pixel-to-pixel variations, and remove significant outliers that were likely unphysical. The variance of the resulting data was computed, and points with a z -score greater than 6 (i.e., points where the value is more than 6σ away from the mean) were flagged as initial seeds for RFI extraction. A two-dimensional watershed algorithm was applied using these seeds as starting points, enlarging the regions of RFI-contamination to neighboring pixels with z -scores greater than 2, until all such pixels were flagged. Figure 4 shows the fractional RFI flag occupancy per time (displayed in LST) and frequency across the 8 days of observations. The majority of the band is relatively clear of RFI. Some clear features are: the FM radio band (below 110 MHz), ORBCOMM satellite communications (137 MHz), an ISS downlink (150 MHz) and VHF TV channels (above 170 MHz)⁷. The galaxy, when transiting zenith at $\text{LST} \approx 17.75$ hours, is so bright that it appears to degrade our ability to flag RFI.

Four antennas were identified during the commissioning as having anomalous behavior. These are marked with red “X”s in Figure 3 and were omitted from further analysis. Before calibration, we manually flagged the edges of the band (below 110 MHz and above 190 MHz), where

⁷ For an extended discussion of RFI as seen by HERA, see the public [HERA Memo #19](#)

spectral behavior is dominated by the high and low pass filtering in the HERA signal chain (DeBoer et al. 2017).

3.2. Calibration

HERA is designed to be calibrated using redundant calibration techniques (Dillon & Parsons 2016), but for this preliminary view of HERA commissioning data, we used image-based calibration. Future studies with deeper integrations targeting EoR detections will take advantage of redundancy to obtain more precise calibration solutions (DeBoer et al. 2017). We used the CASA (McMullin et al. 2007) package for calibration, taking advantage of its CLEAN, gaincal and bandpass functions. We first converted from HERA’s native MIRIAD to a UVFITS file format using PYUVDATA (Hazelton et al. 2017); this could then be ingested by CASA.

The brightest calibration sources near the Dec -30° stripe – for example, those used in previous PAPER analyses like Pictor A (Jacobs et al. 2013) – were not available for this observing window (10.5 - 23 h RA), and the few long baselines in the array available made calibration using individual fainter point sources difficult. We therefore developed a calibration method using the Galactic Center (GC; taken to be at $\alpha, \delta = 17^{\text{h}} 45^{\text{m}} 40^{\text{s}}$, $-29^{\circ} 0^{\text{m}} 28^{\text{s}}$) as modeled by the GSM. Specifically, we selected four minutes of data centered at the transit of the GC to use for calibration. The visibilities were phased from drift-scan mode to a single phase center chosen to be the LST at the start of the observations. Because this phasing imperfectly approximates the tracking telescope assumed by CASA, the length of the observation was chosen to minimize the effects of beam-dependent gain variations as the GC transited. The calibration was done as a two-step process. First, we built an initial model with the GC as an unpolarized, flat-spectrum source with flux density scaled to a reference point of 1 Jy. This allowed us to solve for the large antenna based delay terms using gaincal (`gaintype='K'`; typically 10’s of ns) and a complex bandpass using bandpass. A single solution was obtained for the 4 minute observation for both calibration types, and for the bandpass a solution was obtained for each unflagged \sim 100 kHz channel, resulting in a complex, frequency-dependent gain for each feed. With this first calibration in place, the second step was to interactively CLEAN the image to obtain a more accurate model of the GC extended structure.

We still assumed an unpolarized source, but allowed multiple components within a two degree radius centered on the GC. This was followed by a second round of delay and bandpass calibration to the multi-component extended model, completely analogous to first round of calibration. At this point, an overall frequency-dependent amplitude was required to scale the gains from the arbitrary 1 Jy normalization. For this we used our simulation of the GC from the GSM (converted to units of Jy) to determine a single, spectrally-smooth function for all antennas to make the spectrum of the observations match the simulations.

Clearly, this is an incomplete calibration model. The assumption that the GC is unpolarized is probably adequate, due to the large optical depth towards the GC (Oppermann et al. 2012) resulting in near-complete depolarization in the plane of the Galaxy (Wolleben et al. 2006). Moreover, we expect significant beam depolarization due to the large solid angle of the synthesized beam (see Table 1). Other assumptions are less obviously correct. The GC structure is only partially modeled, and we have assumed the GSM provides an accurate calibration. We have also assumed that the direction-independent Jones matrix is diagonal. Although in principal CASA is capable of solving for D -terms using the `polcal` task, we did not find that the solutions obtained using only an unpolarized GC model were stable or improved the image quality. The lack of polarized point sources as calibrators limits our interpretive power for addressing some aspects of polarization leakage, which we discuss in Section 4.

The calibration we have obtained serves to correct an initial large cable delay per antenna, which aligns all of the power spectra at zero delay, and sets the overall flux scale. The resulting complex antenna-based gains are shown in Figure 5. The gain amplitudes are clearly very similar in shape, with one outlier, and they cluster with 25% of each other. After removing the phase due to the delay term, the resulting phases show only small variations around their mean. The derived bandpasses are clearly spectrally smooth, and thus, even if there are errors, we expect that they will not add additional spectral structure to the power spectrum (see Section 3.3). These gains were applied to all 8 nights of observations. It was found that this produced

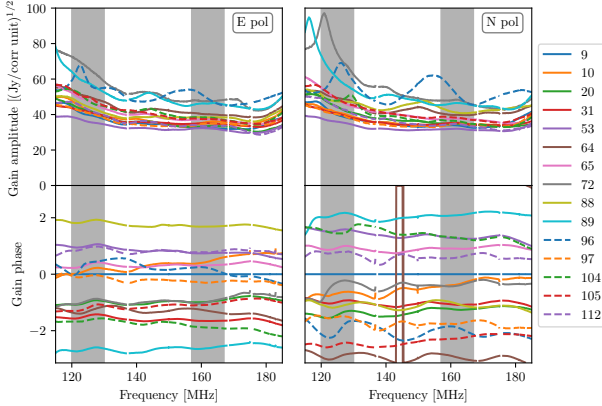


Figure 5. Bandpass solutions obtained for both dipole orientations for all functioning antennas in the array on JD 2457548, and subsequently applied to all data. Each antenna is marked by a different line color and style. Shaded regions indicate the effective sub-bands (the 10 MHz at the center of the 20 MHz Blackman-Harris window) used for power spectrum analysis. The phase is shown after the removal of the delay term.

smaller day-to-day calibration variability than calibrating each day separately to the GC. An estimate of the remaining variation is discussed in Section 4.3.

Figure 6 shows the effect of calibration on the visibilities of three nominally redundantly-spaced baselines. Shown in that figure are the phases of three V^{nn} visibilities from 14.7 m baselines before and after calibration. There were no shared antennas between the visibilities shown. The qualitative agreement is obvious, providing a consistency check on the solutions, and showing our sky-based model achieves redundancy without assuming it. However, small-scale variations between baselines are still seen. This is not unexpected; the antennas are likely to be non-identical, and we have evidence based on closure phase (which is insensitive to calibration errors) that redundant baselines do not see the sky identically (Carilli et al. 2018).

In Figure 7, we show images formed from the simulated pseudo-Stokes visibilities (top panels) and our observations (bottom panels). These are multi-frequency synthesis images, where we used all unflagged frequencies on either side of the band edges, from 115 MHz to 188 MHz. The primary beam has not been deconvolved. All images shown were produced using the same four minute interval used for calibration. Note that at HERA’s latitude the Galactic Center tran-

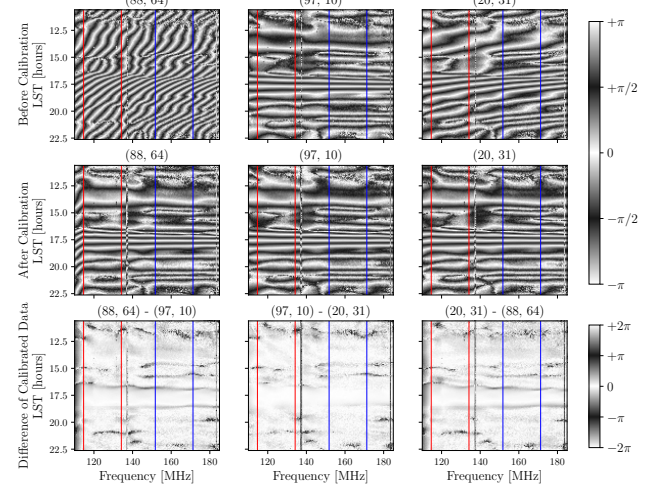


Figure 6. The effect of calibration on the phases of visibilities from three redundantly-spaced 14.7 m baselines; nn polarization. The antenna numbers refer to those given in Figure 3. The color scale is cyclic; black is $\pm\pi/2$ and white is 0 and $\pm\pi$. The extend of the low band is indicated with red lines and the high band with blue. *Top row:* before calibration; *Middle row:* after calibration; *Bottom row:* the three pairs of differences of the calibrated phases. Note that the agreement between baselines is excellent near the Galactic Center but shows significant differences at some other times.

sits 2° north of zenith, while the HERA primary beam has a FWHM of $\sim 10^\circ$ at 150 MHz (Neben et al. 2016). For the simulated visibilities, we flagged the same antennas and channels as in the data. As expected for a compact array, the Stokes I images capture only a low-resolution view of the Galactic Center. The simulated and observed visibilities form remarkably similar images in Stokes I, and Q and U clearly share features in common, due to leakage from I to Q and U through the primary beam (recall that the simulations are unpolarized). In Stokes V, the simulation notably does not reproduce the image well. The presence of emission at the location of the Galactic Center not due to primary beam leakage is consistent with direction-independent gain errors at the few percent level in amplitude (for Stokes Q) and D-terms at $\sim 1\%$ relative to the diagonal gains (for Stokes V) (Thompson et al. 2008). Note that the Stokes U image is broadly consistent with a large fraction of power coming from I leakage through the primary beam, though there is some additional power as well. We consider the implications for the power spectrum in Section 4.

3.3. Forming power spectra

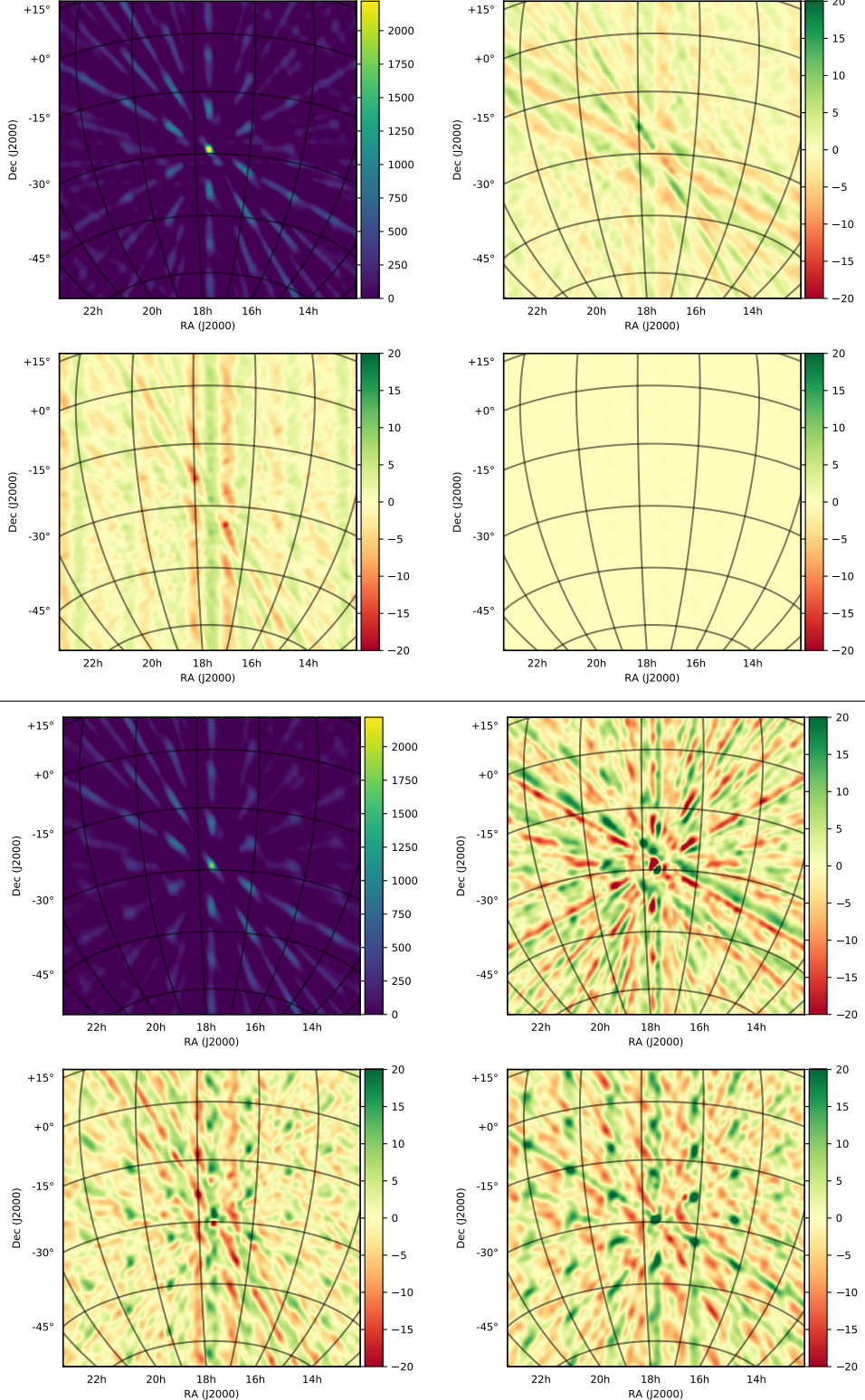


Figure 7. Both sets of panels show multi-frequency synthesis pseudo-Stokes images of I, Q, U and V visibilities (*top left, top right, lower left, lower right*) for the Galactic Center (our calibration source) at transit. Note the field-of-view shown is about 60° across. A Briggs-weighting with robustness 0 was used when gridding into the image plane. No deconvolution was performed. The colorbar is in units of Jy/Beam. A separate color scale is used for Stokes I for suitable dynamic range in the polarized fluxes; note that the color scales differ by a factor of 100. *Above:* Simulation, where only a Stokes I sky was used; any polarized power is due to direction-dependent polarization leakage (see Section 2.1). *Below:* Multi-frequency synthesis pseudo-Stokes images formed from observed visibilities on JD 2457548.

Power spectra were formed in a fashion similar to the method used in Pober et al. (2013) and Kohn et al. (2016). The actual implementation of the code is available as part the GitHub HERA-Team repository `hera_pspec`. We briefly review the method here.

Parsons et al. (2012b) define the *delay transform* as the Fourier transform of a visibility for baseline ij and pseudo-Stokes parameter P along the frequency axis

$$\tilde{V}_{ij}^P(\tau, t) = \int d\nu \tilde{V}_{ij}^P(\nu, t) e^{2\pi i \nu \tau}. \quad (11)$$

We selected two relatively RFI-free 20 MHz sub-bands (Figure 4); 115 to 135 MHz and 152 to 172 MHz, henceforth referred to the “low band” and the “high band” in which to compute the power spectrum. An extremely conservative cut on RFI was used such that any integration which had RFI flagged in the 20 MHz sub-band was excluded from the analysis. This cut was performed separately for the two bands. In each case, approximately 35% of the data was retained after this cut. The bands were then multiplied by a Blackman-Harris window, centered on their central frequencies, before Fourier transforming, in order to minimize side-lobes. This windowing led to an noise-effective bandwidth of 10 MHz. We note that this bandwidth is appropriate for EoR analyses since the H α signal is, to a reasonable approximation, coeval over the corresponding redshift range (Furlanetto et al. 2006). However, this resolution (approximately 100 ns in delay as compared to 194 ns for the longest baseline in this study) does limit our ability to resolve certain features in the power spectrum. We also note that using a Blackman-Harris window will induce a correlation between adjacent τ modes; this should be borne in mind when interpreting plots, as all delay bins are plotted.

The power at each delay-mode and baseline can be represented in terms of their respective Fourier components k_{\parallel} and k_{\perp} (Parsons et al.

2012b; Thyagarajan et al. 2015a):

$$P(k_{\parallel}, k_{\perp}) \approx |\tilde{V}_{ij}^P(\tau)|^2 \frac{X^2 Y}{\Omega_{pp} B_{pp}} \left(\frac{c^2}{2k_B \nu^2} \right)^2,$$

$$k_{\parallel} = \frac{2\pi\nu_{21\text{cm}}H(z)}{c(1+z)^2}\tau,$$

$$k_{\perp} = \frac{2\pi}{D(z)\lambda}b$$

(12)

for: cosmological bandwidth B_{pp} and cosmological angular area of the beam Ω_{pp} , $\nu_{21\text{cm}} \approx 1420$ MHz, baseline length b , wavelength of observation λ , Hubble parameter $H(z)$, transverse comoving distance $D(z)$ and redshift-dependent scalars X and Y (Parsons et al. 2012a). Note that the angular area of the beam refers to the diagonal components of the Mueller matrices shown in Figure 1. For further discussion of forming polarized power spectra in k -space, refer to Nunhokee et al. (2017).

To avoid a noise bias when forming the power spectrum, we cross-multiplied consecutive integrations (each having independent noise), rephasing the zenith angle of the latter to the former:

$$|\tilde{V}_{ij}^P(\tau, t)|^2 \approx |\tilde{V}_{ij}^P(\tau, t) \times \tilde{V}_{ij}^P(\tau, t + \Delta t) e^{i\theta_{ij,\text{zen}}(\Delta t)}| \quad (13)$$

where $\theta_{ij,\text{zen}}(\Delta t)$ was the appropriate phasing for baseline ij and $\Delta t = 10.7$ seconds.

Pseudo-stokes power spectra were formed for each pair of integrations, for every baseline, according to Equation 13. Power spectra from baselines of identical lengths were then averaged together for all observation times over 8 days. The resulting “1D” power spectra for each baseline length were then concatenated to form a two-dimensional power spectrum (that is, arranged into the $(k_{\perp}, k_{\parallel})$ plane). Note that all averaging in this study was performed *after* forming power spectra, *not* by averaging visibilities; this incoherent averaging is non-optimal for achieving the greatest sensitivity. Future work will be able to test the features of the polarized beam and foregrounds too much greater depth.

4. RESULTS

The power spectra formed from the above procedure are shown for all pseudo-Stokes param-

ters for the high and low bands in Figures 8 and 9, respectively.

4.1. General features of the power spectra

Several features of the power spectra are readily apparent. The first is that foreground emission appears in a relatively narrow band near $k_{\parallel} = 0$. Another is that the shape of the power spectrum as a function of k_{\parallel} is both sharply peaked and relatively featureless. We note that a similar study of 2D polarized power spectra in Kohn et al. (2016), PAPER measurements showed a comparably “filled” region of Fourier space out to the horizon delay (i.e., to directions corresponding to zenith angle $\pm 90^\circ$), with some supra-horizon leakage (e.g., Poher et al. 2013) into the EoR window itself. The power spectra in Figures 8 and 9 show similar behavior, though in this case part of the reason is the low resolution (~ 100 ns; see Section 3.3) of the delay transform (Equation 11) due to the small spectral bandwidth, and the small horizon delay associated with the short baselines of the array. Thus we are not able to verify the prediction of Thyagarajan et al. (2015a) and Neben et al. (2016) that for dishes such as HERA, the region between a delay of about 50 ns (set by the width of the antenna primary beam) and the horizon should be free of foreground emission. Similarly, an “excess” of power near the horizon delay, as predicted by the same authors, is not observable, again due to the blurring of features in k_{\parallel} by the resolution. Along the k_{\perp} direction in Stokes I, the amplitude declines as a function of k_{\perp} , as expected for diffuse Galactic emission with a power law angular power spectrum (larger fluctuation power on large scales). This trend is also observed for the other Stokes parameters as well.

A notable feature in the observational data is a peak in power above the noise level at a delay of ~ 1000 ns, independent of the baseline length or the frequency band. There are ~ 150 m coaxial cables connecting the HERA dishes to the correlator⁸ and we have evidence that some of this power is due to a cable reflection at this stage of the signal chain producing an alias of the

foreground signal; see HERA Memo #39 (Ewall-Wice 2017). However, this signal should appear at a delay corresponding to 1300 ns, or twice the propagation time in the coaxial cable. It appears that most of the signal present here is present at a smaller delay, and its origin is not understood.

4.2. Comparison to Simulations

We show a direct comparison between the power spectra of the data and the simulations for the shortest baseline length and all Stokes parameters for both bands in Figure 10 and a zoom-in near close to the wedge in Figure 11. Recall that the simulations include only a Stokes I sky component and no simulated calibration errors, so the only signal in the simulated pseudo-Stokes Q, U, and V power spectra are solely due to wide-field beam leakage (Figure 1). The simulations also only included the diffuse emission of (the most recent version of the GSM; Zheng et al. 2017), which should be accurate at the scales probed by a 14.7 m baseline, but does neglect power from point sources. The power spectra of the simulated data have been computed in the same way as the data.

In comparing to the foreground simulations, there are two things to notice. The first is the *isolation*, or the degree to which the foregrounds remain within the range of k_{\parallel} defined by their intrinsic smoothness and by the mode-mixing of the interferometer, and which can be characterized by the width of the foregrounds in k_{\parallel} (or τ) space. The second is the *dynamic range*, defined here as the ratio between the $k_{\parallel} = 0$ peak and smallest value of the power spectrum. This smallest value may be limited either by noise (in the case of the data) or by the Blackman-Harris window (for the noise-free simulations). We note that the simulations provide a reasonable standard by which to judge both isolation and dynamic range: in the absence of any systematic effects, the width of the foregrounds in delay space cannot be narrower than that captured by the simulated foreground spectral structure and instrument mode-mixing, and the dynamic range is as expected from the window function. Thus over a range of about 8 orders of magnitude in the Stokes I power spectrum, limited by the noise in the data, the isolation in the data agrees well with the simulation, arguing that the calibrated data do not have significant spectral structure beyond that intrinsically present. It

⁸ This stage of the signal chain is only present in the commissioning array. Future HERA build-outs will transition to a different architecture using RF over fiber with long fiber runs to move this signal to even longer delays (DeBoer et al. 2017).

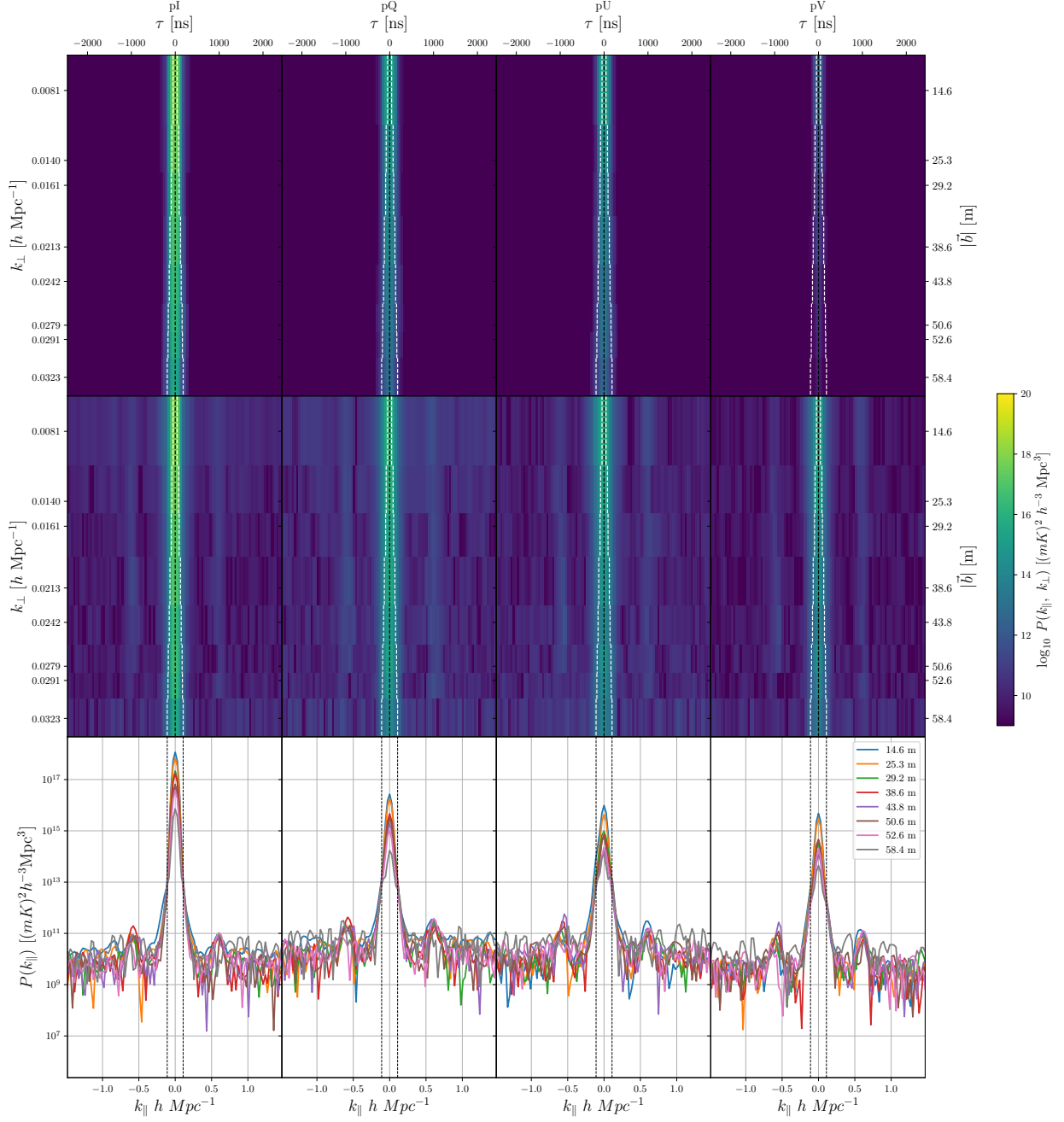


Figure 8. Results from the high-band (157–167 MHz). *Top:* Simulated power spectra in Stokes I, Q, U and V, following the formalism in Section 2. No polarized sky model was used, so power in Stokes Q, U and V is only due to the direction-dependent beam leakage from Stokes I. No instrumental noise was included in the simulation. *Middle:* Eight-day average power spectra from data. *Bottom:* The same data as shown in the middle panel, but with each baseline length overlaid on one another to allow shared features to be more easily identified. For the top and middle plots, white dotted lines indicate the boundary of the pitchfork and the EoR window for that baseline length. A black dotted line indicates the $k_{\parallel} = 0 \text{ h/Mpc}$ line. In the bottom panel, dotted lines indicate the boundary of the wedge for the longest baseline only. Delays in nanoseconds are indicated along the top, and the corresponding cosmological k at the mean redshift along the bottom axis.

is worth pointing out there is some evidence for broadening of the range in k near the noise floor. For the other pseudo-Stokes spectra, the isolation is worse: the power spectrum of the data is noticeably wider than the simulation.

Referring to Figure 11, it is clear that the calibration to the simulation described in Section 3.2 was imperfect: in both bands, the amplitude of the real data is 60 - 80% of the simulated value in the pseudo-Stokes I power spectrum. This is consistent with calibration derived from the GC agreeing between the simulation and data to $\sim 10\%$.

The comparison of the simulation to the other pseudo-Stokes parameters is more telling: the beam leakage modeled in the simulation is of roughly equal magnitude for both Q and U in both bands, but the data show a markedly stronger pseudo-Q than U in both bands. Since there is no strong reason to believe the sky is highly anisotropic between Q and U over the range of RA included here, this argues for another interpretation. Indeed, gain errors between the E and N polarized feeds of about 10% would account for I to Q leakage of the magnitude seen. In the high band, the simulated polarized leakage appears to account for nearly all of the observed power in U, but not in the low band.

Interpreting the measured pseudo-Stokes Q and U power spectra as detections of actual polarized power would require polarized fractions in Stokes Q and U images order 5 - 20%. This is on the high end of range of measurements of $\sim 1.6 - 4.5\%$ fractional polarization at 150 MHz on large-scale polarized structures by Jelić et al. (2015) and Lenc et al. (2016). We note that whatever the interpretation of the linear pseudo-Stokes spectra, they do not provide strong evidence for high rotation measure emission, which would be present at $k_{\parallel} > 0.1$ for $RM > 10 \text{ rad m}^{-2}$ in the high band Moore et al. (2017), although noise prevents probing levels as deep as those in Asad et al. (2018).

The observed pseudo-Stokes V power spectrum was more poorly modeled by our simulation. In both bands we observed ~ 20 dB more power in pseudo-Stokes V at $k_{\parallel} = 0 \text{ h/Mpc}$ than predicted by our simulations. The peak power observed in pseudo-Stokes V was roughly 0.1% of the peak power observed in pseudo-Stokes I, comparable to the power in pseudo-Stokes Q and U. Since

we do not expect any significant circular polarization from the sky, a more likely explanation here direction independent leakage, in the form of Jones matrix D -terms of $\sim 1\%$ (Thompson et al. 2008). This is similar to D -term levels from other low frequency instruments such as MWA-32, which was found to have $\sim 2\%$ D -terms (G. Bernardi, private communication).

4.3. Noise Levels

One estimate of the system temperature of the observations was formed from the calibrated values of the auto-correlations. These were compared against the values obtained from the simulation. Over the RA range observed, which was heavily weighted towards the Galactic Center and much of the Galactic Plane, the system temperature estimated in this way was 1230 K for the high band and 4000 K for the low band, which was consistent with the simulated autocorrelations (DeBoer et al. 2017, also see the public HERA Memo #16).

The system temperature was converted to a noise level in the power spectrum according to the formalism in Parsons et al. (2012b), with the inclusion of a baseline-number dependence:

$$P_{\text{Noise}}(k) \approx \frac{1}{2\Delta t \sqrt{N_{\text{LST}}} N_{\text{days}} N_{\text{bl}}} X^2 Y B_{\text{NE}} \Omega_{\text{eff}} T_{\text{sys}}^2. \quad (14)$$

In the above equation, Δt is integration time, N_{LST} is the number of LST hours used per day (12 hours), N_{bl} is the number of baselines (which differed per k_{\perp} bin), X and Y are cosmological scalars defined in Parsons et al. (2012b), B_{NE} is the noise equivalent bandwidth and Ω_{eff} is the effective beam area, as defined in Parsons et al. (2014). Figure 12 shows power as a function of baseline length for $k_{\parallel} = 0 \text{ h/Mpc}$ (solid lines) and the average over $|k_{\parallel}| > 1 \text{ h/Mpc}$ (dot-dashed lines). Though not shown in Figures 8 and 9, the frequency sampling of the instrument is sensitive to delays up to 5000 ns, and this region defines our white noise level. To match the observed noise level of the power spectrum in Stokes I, high band, required an assumed system temperature of 2400 K, higher than that expected based on the sky and beam model from the simulations, or from the measured calibrated autocorrelations. The cause of this excess is not understood. Figure 12 also shows that both the noise and calibration of the instrument were stable at

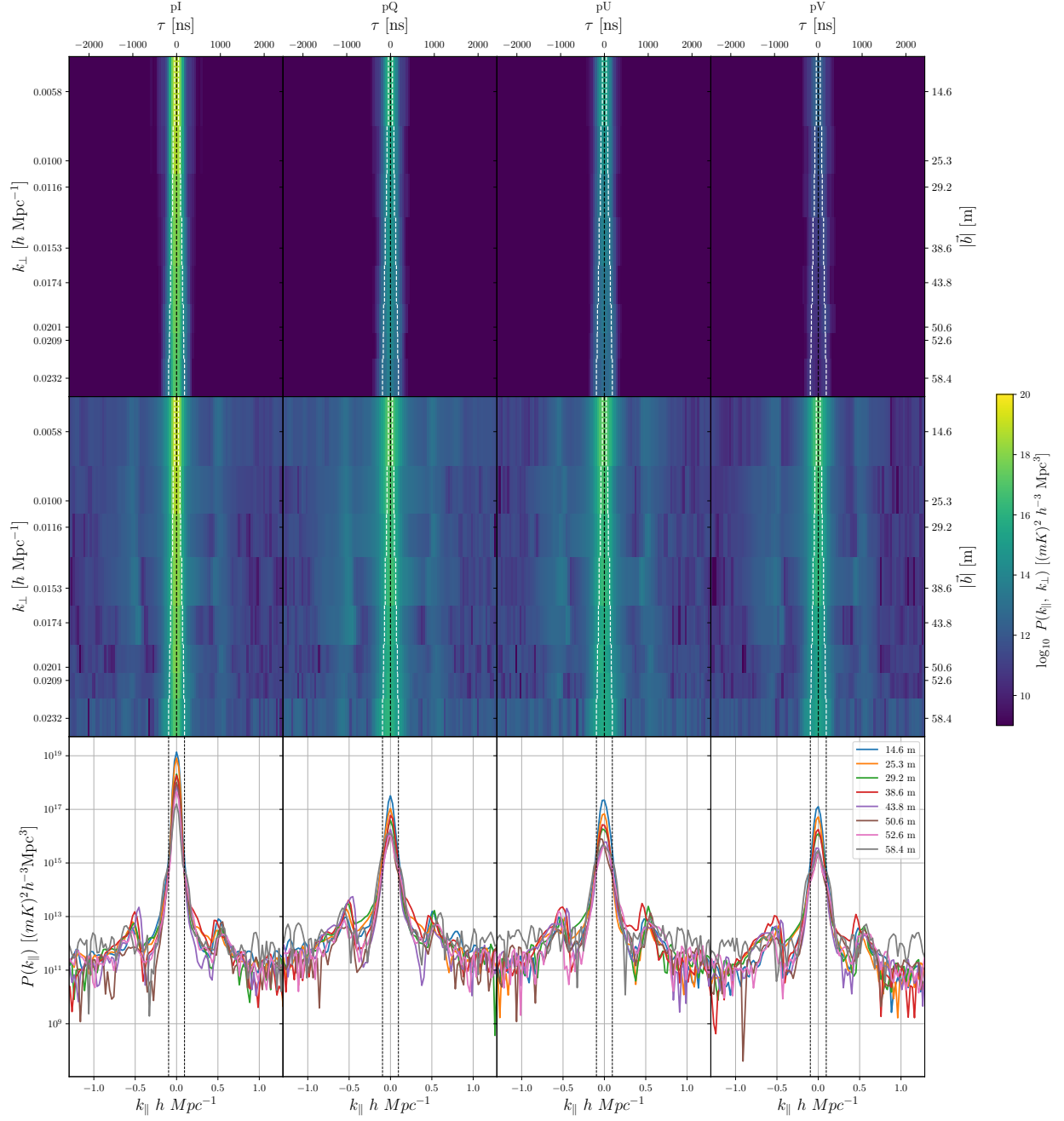


Figure 9. Results from the low-band (120–130 MHz), arranged in the same format as Figure 8.

the 20% level in the visibilities (50% in the power spectrum) over the 8 days presented here.

5. CONCLUSIONS

In this work we have investigated the polarization response of the HERA-19 commissioning array, both in imaging and particularly in the power spectrum domain. We find that a simple image-based calibration based on the unpolarized diffuse emission of the Global Sky Model (GSM) has a spectrally smooth structure and achieves qualitative redundancy between the nominally-redundant baselines of the array. We are able to calibrate the data based on the Galactic Center observations to the GSM with an accuracy of about 10%, and about 20% variation from day-to-day.

Forming power spectra in all pseudo-Stokes parameters, we show that we achieve isolation of the foregrounds in Stokes I as expected due to their intrinsic spectral smoothness, the modeled instrument chromaticity, and the calibration, limited in dynamic range by the noise. Excess power at a delay of ~ 1000 ns is seen in all polarizations which may in part be due to cable reflections, but is not fully explained. Excess power is also seen in the power spectra of the linear polarization Stokes parameters which is not easily attributable to leakage via the primary beam, and results from some combination of residual calibration errors and actual polarized emission. Finally, Stokes V is found to be highly discrepant from the expectation of zero power, likely due to the lack of calibration of off-diagonal Jones matrix (“D”) terms.

The results presented here are necessarily preliminary, and point in obvious directions for improvements in the quality of calibration, particularly the polarized calibration, which are currently being prepared by the HERA collaboration. Deeper integrations no the power spectrum will probe the structure of the foregrounds and instrument response to a higher dynamic range and over a wider range in k_{\perp} -modes as more antennas are added, allowing a more thorough characterization of the wedge shape. A build-out of HERA to 350 antennas with a new broad-band feed and completely new electronics chain is now underway DeBoer et al. (2017), with strong quality-assurance efforts informed in part by this analysis.

Much of this study was undertaken during the inaugural CAMPARE-HERA Astronomy Minority Partnership (CHAMP). This material is based upon work supported by the National Science Foundation under Grant Nos. 1440343 and 1636646, the Gordon and Betty Moore Foundation, and institutional support from the HERA collaboration partners. SAK is supported by a University of Pennsylvania SAS Dissertation Completion Fellowship. JEA acknowledges support from NSF CAREER award # 1455151. C.D.N. is supported by the SKA SA scholarship program. AL acknowledges support for this work by NASA through Hubble Fellowship grant # HST-HF2-51363.001-A awarded by the Space Telescope Science Institute, which is operated by the Association of Universities for Research in Astronomy, Inc., for NASA, under contract NAS5-26555. G.B. acknowledges support from the Royal Society and the Newton Fund under grant NA150184. This work is based on the research supported in part by the National Research Foundation of South Africa (grant No. 103424). JSD acknowledges the support of the NSF AAPF award # 1701536 and the Berkeley Center for Cosmological Physics.

We thank the anonymous referee for many helpful suggestions.

Software: This research made use of Astropy, a community-developed core Python package for Astronomy (Astropy Collaboration et al. 2013); CASA (McMullin et al. 2007); pyuvdata (Hazelton et al. 2017); pygsm (Price 2016)

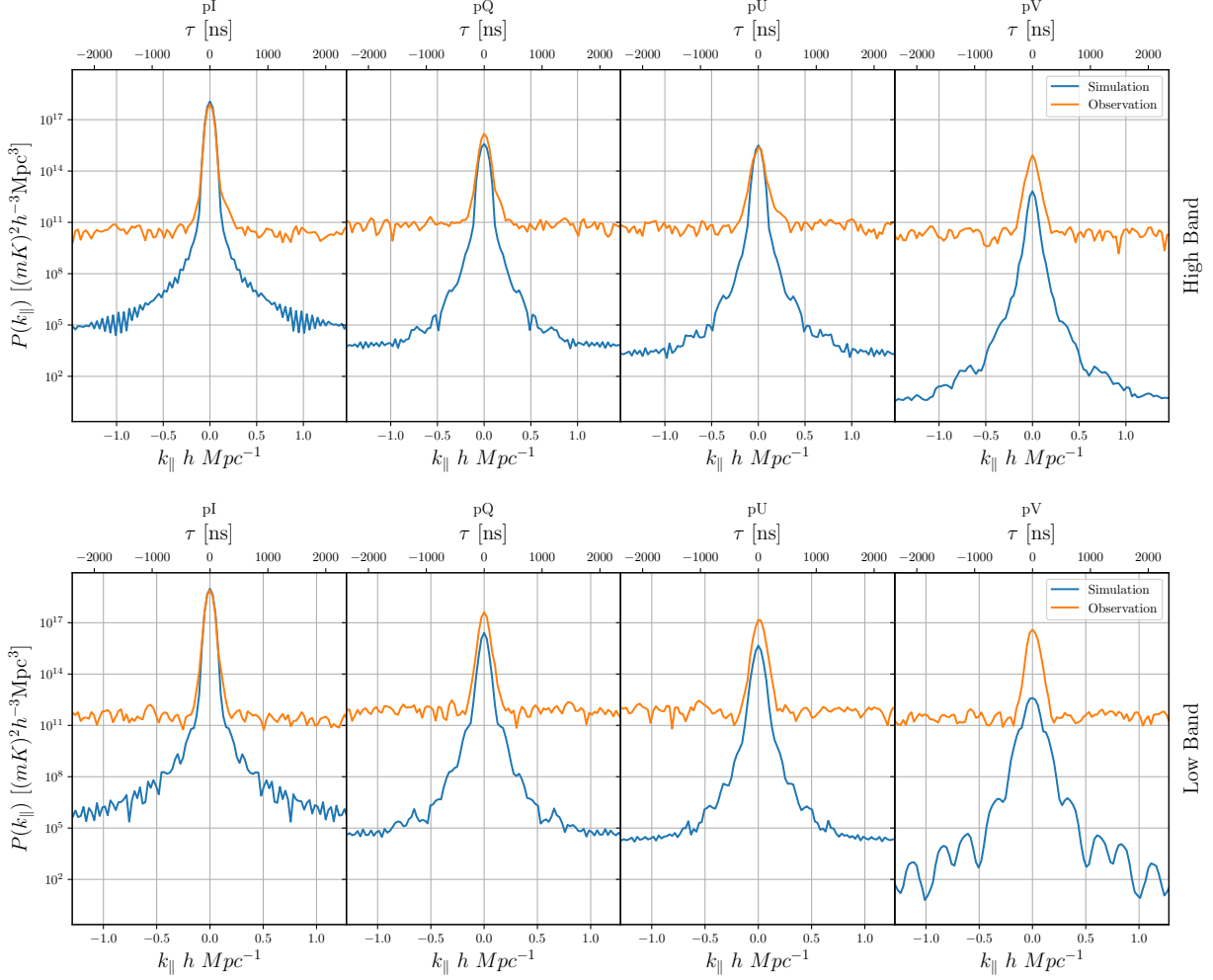


Figure 10. Simulated and observed power as a function of k_{\parallel} for the shortest baseline (14.6 m). *Right to left:* pseudo-Stokes I, Q, U and V; *above:* the high band; *below:* the low band. The simulations were noiseless and used an unpolarized sky model. The agreement with Stokes I is consistent with an absolute calibration accuracy of $\sim 10\%$. The agreement between the simulations and the data for the other pseudo-Stokes parameters is poor, as discussed in the text, likely due to a combination of calibration errors, particularly for Stokes V, and actual polarized emission.

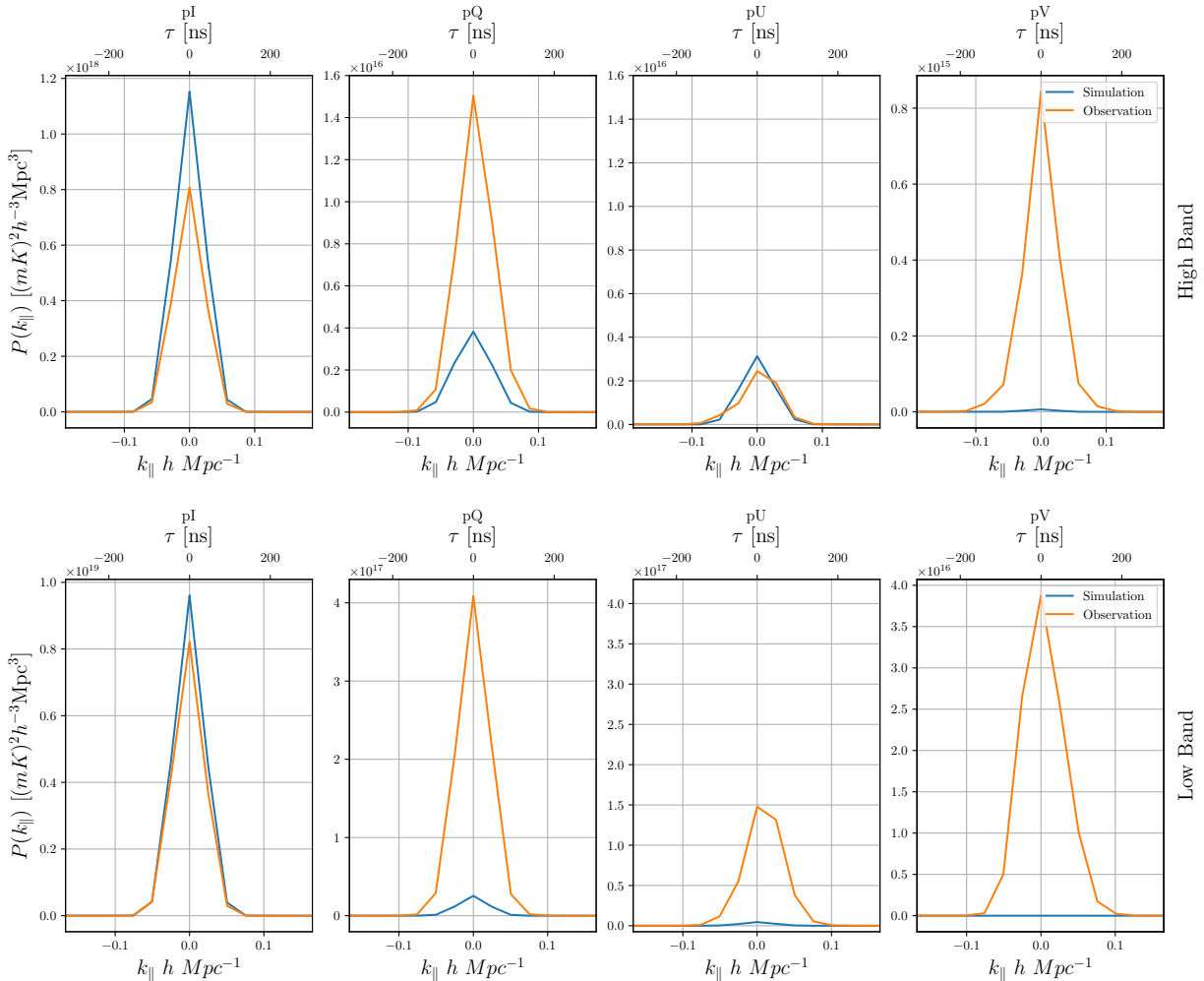


Figure 11. A zoom in on Figure 10 showing just the k values near the wedge, and with a linear scale in $P(k_{\parallel})$. Note that the scale changes for each Stokes for each parameter, except that Q and U are set to have the same scale in each row.

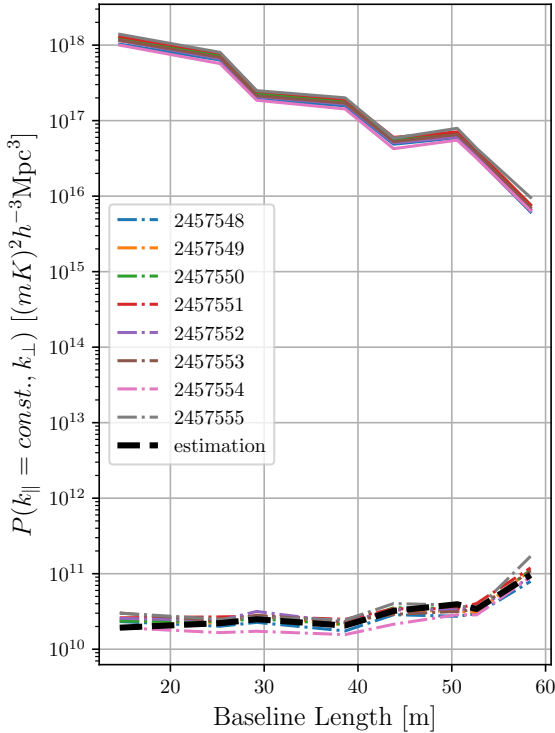


Figure 12. High band power as a function of baseline length for $k_{\parallel} = 0$ h/Mpc (solid lines) and an average value over the white noise ($|k_{\parallel}| > 1$ h/Mpc; dot-dashed lines) for pseudo-Stokes I on each JD of observation. The black dashed line represents estimated power spectrum noise given a system temperature of 2400 K. A very similar relationship obtains for the low band (not shown), but with a higher system temperature of 7000 K. Note that the increase of the noise level with baseline length is correctly modeled, as the compact array has a decreasing number of baselines which are averaged together in a given $(k_{\parallel}, k_{\perp})$ bin.

REFERENCES

- Asad, K. M. B., Koopmans, L. V. E., Jelić, V., et al. 2018, MNRAS, 476, 3051
- . 2015, MNRAS, 451, 3709
- . 2016, MNRAS, 462, 4482
- Astropy Collaboration, Robitaille, T. P., Tollerud, E. J., et al. 2013, A&A, 558, A33
- Bernardi, G., de Bruyn, A. G., Brentjens, M. A., et al. 2009a, A&A, 500, 965
- . 2009b, A&A, 500, 965
- Bernardi, G., de Bruyn, A. G., Harker, G., et al. 2010, A&A, 522, A67
- Bernardi, G., Greenhill, L. J., Mitchell, D. A., et al. 2013, ApJ, 771, 105
- Carilli, C. L., Nikolic, B., Thyagarayan, N., et al. 2018, Radio Science, 53, 845
- Carozzi, T. D., & Woan, G. 2009, MNRAS, 395
- Datta, A., Bowman, J. D., & Carilli, C. L. 2010, ApJ, 724, 526
- de Oliveira-Costa, A., Tegmark, M., Gaensler, B. M., et al. 2008, MNRAS, 388, 247
- DeBoer, D. R., Parsons, A. R., Aguirre, J. E., et al. 2017, PASP, 129, 045001
- Dillon, J. S., & Parsons, A. R. 2016, ApJ, 826, 181
- Dillon, J. S., Liu, A., Williams, C. L., et al. 2014, PhRvD, 89, 023002
- Dillon, J. S., Neben, A. R., Hewitt, J. N., et al. 2015a, PhRvD, 91, 123011
- Dillon, J. S., Tegmark, M., Liu, A., et al. 2015b, PhRvD, 91, 023002
- Ewall-Wice, A. 2017, A Survey of HERA HC1 150 m cable reflections, Tech. rep., HERA Memo Series #39
<http://reionization.org/science/memos/>
- Ewall-Wice, A., Bradley, R., Deboer, D., et al. 2016, ApJ, 831, 196
- Fagnoni, N., & de Lera Acedo, E. 2016, ArXiv e-prints, arXiv:1606.08701
- Farnes, J. S., Gaensler, B. M., & Carretti, E. 2014, ApJS, 212, 15
- Furlanetto, S. R., Oh, S. P., & Briggs, F. H. 2006, PhR, 433, 181
- Geil, P. M., Gaensler, B. M., & Wyithe, J. S. B. 2011, MNRAS, 418, 516
- Hazelton, B., Beardsley, A., Pober, J., et al. 2017, HERA-Team/pyuvddata: Version 1.1, doi:10.5281/zenodo.546260
- Jacobs, D. C., Parsons, A. R., Aguirre, J. E., et al. 2013, ApJ, 776, 108
- Jelić, V., de Bruyn, A. G., Mevius, M., et al. 2014, A&A, 568, A101
- Jelić, V., de Bruyn, A. G., Pandey, V. N., et al. 2015, A&A, 583, A137
- Kohn, S. A., Aguirre, J. E., Nunhokee, C. D., et al. 2016, ApJ, 823, 88
- Lenc, E., Gaensler, B. M., Sun, X. H., et al. 2016, ApJ, 830, 38
- Lenc, E., Anderson, C. S., Barry, N., et al. 2017, PASA, 34, e040
- Liu, A., Parsons, A. R., & Trott, C. M. 2014a, PhRvD, 90, 023018
- . 2014b, PhRvD, 90, 023019
- Ludwig, A. 1973, IEEE Transactions on Antennas and Propagation, 21, 116
- Martinot, Z. E., Aguirre, J. E., Kohn, S. A., & Washington, I. Q. 2018, ApJ, 869, 79
- McMullin, J. P., Waters, B., Schiebel, D., Young, W., & Golap, K. 2007, in Astronomical Data Analysis Software and Systems XVI, ed. R. A. Shaw, F. Hill, & D. J. Bell, 376, ASP, San Francisco, CA, 127
- Moore, D. F., Aguirre, J. E., Parsons, A. R., Jacobs, D. C., & Pober, J. C. 2013, ApJ, 769, 154
- Moore, D. F., Aguirre, J. E., Kohn, S. A., et al. 2017, ApJ, 836, 154
- Morales, M. F., Hazelton, B., Sullivan, I., & Beardsley, A. 2012, ApJ, 752, 137
- Neben, A. R., Bradley, R. F., Hewitt, J. N., et al. 2016, ApJ, 826, 199
- Nunhokee, C. D., Bernardi, G., Kohn, S. A., et al. 2017, ApJ, 848, 47
- Oppermann, N., Junklewitz, H., Robbers, G., et al. 2012, A&A, 542, A93
- Parsons, A., Pober, J., McQuinn, M., Jacobs, D., & Aguirre, J. 2012a, ApJ, 753, 81
- Parsons, A. R., Pober, J. C., Aguirre, J. E., et al. 2012b, ApJ, 756, 165
- Parsons, A. R., Backer, D. C., Foster, G. S., et al. 2010, AJ, 139, 1468
- Parsons, A. R., Liu, A., Aguirre, J. E., et al. 2014, ApJ, 788, 106
- Planck Collaboration, Ade, P. A. R., Aghanim, N., et al. 2016, A&A, 594, A13
- Pober, J. C., Parsons, A. R., Aguirre, J. E., et al. 2013, ApJL, 768, L36
- Pober, J. C., Liu, A., Dillon, J. S., et al. 2014, ApJ, 782, 66
- Price, D. C. 2016, PyGSM: Python interface to the Global Sky Model, Astrophysics Source Code Library, ascl:1603.013
- Shaw, J. R., Sigurdson, K., Sitwell, M., Stebbins, A., & Pen, U.-L. 2015, PhRvD, 91, 083514

- Smirnov, O. M. 2011a, A& A, 527, A106
 —. 2011b, A& A, 527, A107
- Thompson, A. R., Moran, J. M., & Swenson Jr, G. W. 2008, Interferometry and synthesis in radio astronomy (John Wiley & Sons)
- Thyagarajan, N., Parsons, A. R., DeBoer, D. R., et al. 2016, ApJ, 825, 9
- Thyagarajan, N., Udaya Shankar, N., Subrahmanyam, R., et al. 2013, ApJ, 776, 6
- Thyagarajan, N., Jacobs, D. C., Bowman, J. D., et al. 2015a, ApJL, 807, L28
 —. 2015b, ApJ, 804, 14
- Trott, C. M., Wayth, R. B., & Tingay, S. J. 2012, ApJ, 757, 101
- van Straten, W., Manchester, R. N., Johnston, S., & Reynolds, J. E. 2010, PASA, 27, 104
- Vedantham, H., Udaya Shankar, N., & Subrahmanyam, R. 2012, ApJ, 745, 176
- Wolleben, M., Landecker, T. L., Reich, W., & Wielebinski, R. 2006, A& A, 448, 411
- Zheng, H., Tegmark, M., Dillon, J. S., et al. 2017, MNRAS, 464, 3486